

A New Instrument for Measurement of the Solar Aureole Radiance Distribution from Unstable Platforms

JOSEPH M. RITTER* AND KENNETH J. VOSS

Physics Department, University of Miami, Coral Gables, Florida

(Manuscript received 11 January 1999, in final form 23 September 1999)

ABSTRACT

A novel imaging solar aureole radiometer, which can obtain absolute radiometric measurements of the solar aureole when operated on an unstable platform, is described. A CCD array is used to image the aureole, while a neutral density occulter on a long pole blocks the direct solar radiation. This ensures accurate direction registration as the sun appears in acquired images, and the total circumsolar region is measured simultaneously. The imaging nature of this instrument along with a special triggering device permit acquisition of the circumsolar sky radiance within 7.5° of the center of the solar disk, and within 1° of the edge of the solar disk. This innovation makes possible, for the first time, reliable and accurate radiometric measurements of the solar aureole from unstable mobile platforms such as ships. This allows determination of the small angle atmospheric light scattering. The instrument has been used in field studies of atmospheric aerosols and will be used in satellite validation and calibration campaigns.

1. Introduction

The solar aureole is the region of enhanced brightness surrounding the sun. This skylight is predominately a result of scattering from large particles (aerosols) in the atmosphere. Aerosols scatter light of wavelength comparable to or smaller than their own size predominantly in the forward direction because of diffraction, causing this region of enhanced brightness. Measurements of the solar aureole can provide information on the large particle fraction of the aerosol size distribution.

Aerosols (solid and liquid particles suspended in the atmosphere) play an important role in determining the earth's radiation budget (and hence its climate), as well as influencing the chemical composition of the gaseous atmosphere. Aerosols can affect the earth radiation budget both directly by scattering and absorbing solar and terrestrial radiation (Charlson et al. 1992) and indirectly by modifying cloud properties through their role as cloud condensation nuclei (Twomey 1977). Unfortunately, the global impact of aerosol optical effects are not well understood. In fact, the uncertainty in the aero-

sol radiative forcing is larger than the uncertainty in climate forcing by all greenhouse gases released over the past century (Houghton et al. 1996). To reduce this uncertainty, improved measurements of aerosol optical properties are needed for aerosol and climate field studies.

Scattering by intervening aerosols provides much of the signal received by earth-viewing satellites (Gordon 1997). Improved understanding of aerosol optical properties is essential to improvement in the interpretation of satellite observations of the earth's surface and to validate remote satellite measurements of ocean and land properties.

Measurements of the sky radiance distribution, excluding the difficult region of the solar aureole, have been made for several years (Zibordi and Voss 1989). These measurements can be used to determine the large angle scattering from aerosols; however, without measuring the solar aureole, no information is available on the small angle scattering. It is therefore important to acquire solar aureole data in order to accurately determine the full aerosol scattering phase function.

Radiometric measurements of the solar aureole, when combined with spectral extinction data, can yield data products such as the aerosol size distribution and the aerosol scattering phase function for small scattering angles (Nakajima et al. 1983, 1996). These measurements when combined with large scattering angle measurements are useful in determining the aerosol single scattering albedo (Wang and Gordon 1993). In addition, ocean color sensor vicarious calibration studies require

* *Current affiliation:* Space Optics Manufacturing Technology Center, Advanced Optical Systems Development, NASA MSFC, Huntsville, Alabama.

Corresponding author address: Space Optics Manufacturing Technology Center, Advanced Optical Systems Development SD 71, NASA MSFC, Huntsville, Alabama 35812.
E-mail: Joe.Ritter@msfc.nasa.gov

sky radiance measurements to be made at sea (Clark et al. 1997).

Direct solar radiation is on the order of a million times the intensity of the solar aureole. This creates additional design challenges. Measurement platform motion coupled with large changes in aureole radiance over small angles requires an instrument with a high signal-to-noise ratio, accurate pointing, fast triggering, short exposure times, low jitter, as well as sensor stability.

Prior to this work, no existing instrumentation had the required capabilities. An imaging radiometer meeting these requirements has been developed and will be described. The imaging nature of the instrument allows measurement of sky radiance within 1° of the center of the solar disk even when deployed on an unstable platform such as a ship.

2. Instrument description

Some previous successful approaches to solar aureole radiometry have involved scanning radiometers on stable platforms (Holben et al. 1996). At sea, platform motion combined with issues of repeatable pointing and tracking required a different approach. One novel characteristic of this instrument is that it acquires the absolute circumsolar sky radiance in a single image using a charge-coupled device (CCD) camera (Ritter et al. 1997a). Use of a camera ensures accurate direction registration as the total circumsolar region is measured simultaneously, and the sun appears as a reference point in acquired images.

The system components are illustrated in Fig. 1. The current configuration employs a cooled 512×512 CCD array, 35-mm lens and filter wheel, internal and external cooling system, sun alignment sensor and optics with associated control, and triggering and digitizing electronics. This package is mounted on a 2-m pole and pointed manually toward the sun. An occulter mounted on the end of the pole attenuates the direct sunlight and shadows the camera aperture prohibiting internal flare. A sun alignment sensor automatically exposes the CCD when the camera orientation is correct. A remote desktop computer performs instrument control and data acquisition. The instrument components are described in the following sections.

a. Occulter

An occulter placed at the end of a 2-m pole shadows the camera aperture so that scattered radiation entering the aperture is a minimum of $\frac{1}{2}^\circ$ off of the instrument optical axis. The solar disk itself only subtends a half-angle of $\frac{1}{4}^\circ$ at the instrument. In the center of the occulter is a neutral density filter that produces an attenuated image of the solar disk, which, when combined with ephemeris data, can be used to determine the azimuth and zenith coordinates corresponding to each CCD pixel. In addition, since the camera, and most of

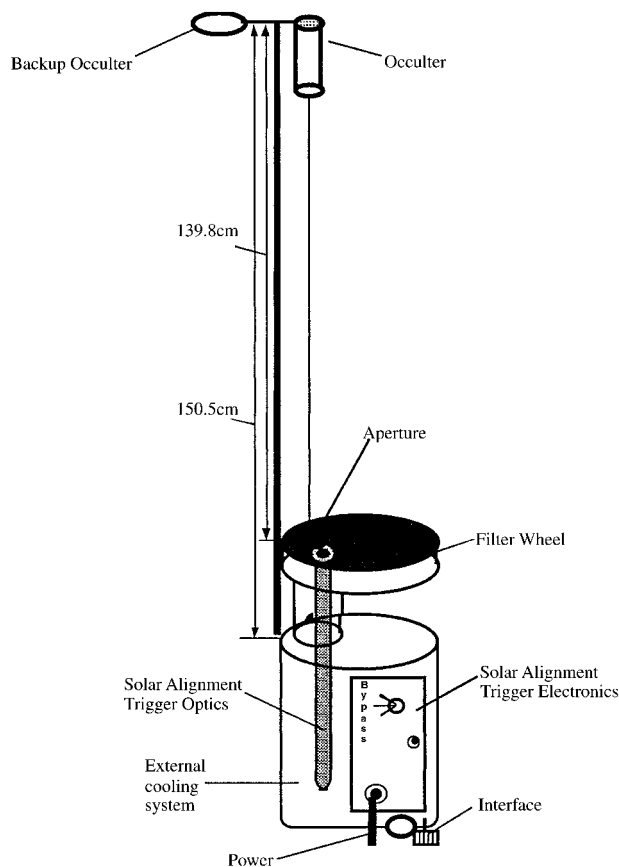


FIG. 1. Schematic of the imaging aureole radiometry system.

the weight of the instrument is below the pole, which holds the occulter, the orientation of the occulter can help to locate the vertical in an image.

b. Filter wheel

After the occulter, the first optical element the light entering the system encounters is the filter wheel housing window. This window is coated with an antireflection coating and has a clear 1-cm inner diameter. Inside the filter wheel housing, 10-nm interference filters centered at 440, 560, 670, and 860 nm are used to limit the spectral bandpass of the instrument. The filter wheel and housing provide an effective light seal with neighboring components without significantly extending the optical path. Since this system is only looking at a narrow angular range around the sun, the variation in bandpass of the filters with variation in the angle of incidence of light being filtered is negligible ($<1\%$ change in center wavelength). Since the filter wheel is not at an image position in the optical system, light entering the system is averaged over the whole filter area, thus the spatial uniformity of the filters is not important.

Each interference filter is paired with a neutral density filter to optimally utilize the available dynamic range of the sensor. Each spectral channel response is adjusted

TABLE 1. Filter specifications. Interference filter centers and FWHM (full-width at half-maximum) bandwidths along with the paired neutral density transmittance.

Filter (nm)	Centroid (nm)	FWHM (nm)	ND transmittance
440	440.9	10	1.000
560	561.3	10	0.0121
670	670.2	12	0.0248
860	856.6	13	0.0478

for near saturation at 1.0° from the center of the solar disk with the exception of the 440-nm channel. The low system response at 440 nm would have required longer exposure times to achieve this, and this could have led to potential blurring effects caused by platform motion. The nominal neutral density filter transmission for each channel is shown in Table 1.

c. Lens

After passing through the interference and neutral density filters the light enters a camera lens. The current lens system is a standard 35-mm Nikkor camera lens with a 50-mm focal length having standard antireflection coatings. Because the CCD array size is smaller than the standard 35-mm film format, and because of other geometrical considerations (e.g., the filter wheel's front aperture diameter), the field of view is reduced from what would be expected with this focal length. In the present configuration the instrument has an angular resolution of 0.05° and a field of view of $\pm 7.5^\circ$ centered on the sun. The angular resolution is more than sufficient for determining the instrument coordinates as well as the photon scattering angle because the finite extent of the solar disk (0.5°) introduces a corresponding uncertainty in measurement of the scattering angle. The camera lens was stopped at the smallest aperture, $f/15$, to reduce aberrations and stray light to a minimum.

d. Shutter

An electromechanical shutter is employed in this system. A computer-controlled integration and shuttering system ensures that the integration time is constant (within $10 \mu\text{s}$) while exposing rapidly enough (19×10^{-3} s) to eliminate image blur due to ship motion. For all calibrations and measurements the shutter is operated at the same speed, thus mechanical movement of the shutter across the array is taken into account during calibration. Quantitative assessment of jitter and other calibration issues are addressed below.

e. Pointing and triggering

An essential feature for shipborne applications is a unique sun-sensing optoelectronic trigger device that trips the camera shutter only when suitable alignment

of the sun with the instrument optical axis is achieved. The trigger developed for this instrument consists of a 30-cm baffled collimating tube with a window and neutral density filter at one end, and a photodiode amplifier package at the other. The axis of the tube is aligned parallel to the optical axis of the aureolemeter. When the tube (and thus the aureolemeter) is aligned with the sun, the photodiode is activated, a pulse is generated, and an audible signal is produced. The pulse is amplified and shaped, then used to trigger the shutter. This scheme allows measurement of the aureole to within 1° of the edge of the solar disk even when deployed on an unstable platform such as a ship. Alignment between the camera and trigger is achieved by adjusting the position of trigger tube until the trigger fires when the occulter shadow falls symmetrically on the filter wheel front aperture. This is done at the beginning of each expedition and can be checked throughout the trip by looking at the individual data images. The system has been used and performed well, even in 60 kt winds during the NASA TARFOX experiment (Ritter et al. 1997a). It should be noted that this ship was partially stabilized by its size (700 ft), but the main source of instrument motion was the wind.

f. Detector

The imaging detector used is a commercially available camera (Spectrasource MCD-1000) that employs a thermoelectrically cooled 512×512 element CCD array (TK512). A 2D array rather than a linear array is desirable for several reasons. The projection of the al-mucantar onto an image plane is described by a conic, whose shape varies with solar zenith angle; therefore, a linear array is less suitable. Two-dimensional arrays are commercially available in developed systems that can be adapted to radiometry. In addition, by using a 2D array rather than a linear array the requirements for pointing accuracy are reduced, as small pointing deviations can be accommodated in the postprocessing of the data. Finally, capturing the full circumsolar image allows for simple screening of data, as most problems (clouds, ship superstructure, etc.) are obvious when images are viewed. Double-correlated sampling digitizes individual pixels at 16-bit resolution. The system provides a total noise variation of less than 11 counts. The array temperature is actively servo-controlled by Peltier cooling. A supplementary external cooling system was constructed to help draw additional heat from the instrument, thus ensuring sensor stability in field deployments.

g. Data acquisition and control

A desktop computer is employed to control data acquisition as well as to perform primary data reduction. Software was written to provide a menu-driven user interface and to control image digitization, storage, and

shuttering, as well as to perform field diagnostics. Interrupt routines were written in native assembly language to accommodate strict timing and repeatability requirements. The software incorporates a control loop allowing complete remote system operation by the experimenter, usually located outdoors with the sensor 50–100 ft from the control system. Complementary instruments are employed to provide optical depth, measurement location, ambient pressure, humidity, and temperature data.

3. Instrument calibration and characterization

There are several calibration steps required to convert the camera output into calibrated sky radiance data. In addition, the electrooptical system has been characterized to understand the performance limitations of the system. These steps are detailed in the following section.

a. Angular calibration

Angular calibration is required to determine the mapping between the image location on the array focal plane and the corresponding angle in real space. The angular calibration was accomplished by placing the instrument on a precision rotary table, imaging a point source, and then acquiring an image. The camera was then rotated by a known angle and another image was acquired. This was done for angles from 0° to 7° . The rotation precision was $\pm 0.25^\circ$. The pixel displacement of the light source in the image was then determined. Each pixel was found to cover a 0.05° wide (full angle) field of view.

b. Dark signal

There are several components of the dark signal, which are not easily separable. An experiment was performed to determine the time-dependent thermally generated dark current and its impact on signal-to-noise degradation. A series of dark images were taken with exposure times ranging from 19×10^{-3} s to 100 s. For each image the average value from 100 pixels in the center of the image was recorded. The slope of the resulting dark signal versus time curve indicated that approximately eight thermal counts per second per pixel are generated at the nominal sensor operating temperature of 252 K. The normal exposure time for a sky image is 19×10^{-3} s, thus these thermal counts become significant only if the CCD is not cleared immediately prior to acquiring an image. In order to achieve a higher dynamic range, the architecture of the TK512 chip is designed in a way that prohibits rapid clearing. The approach of continuously clocking out charge from the chip one line at a time prior to exposing was adopted to solve both of these problems. There is also a position-dependent dark signal, a result of pixel-to-pixel bias variations as well as local fabrication differences. Immediately following acquisition of each sky image, a

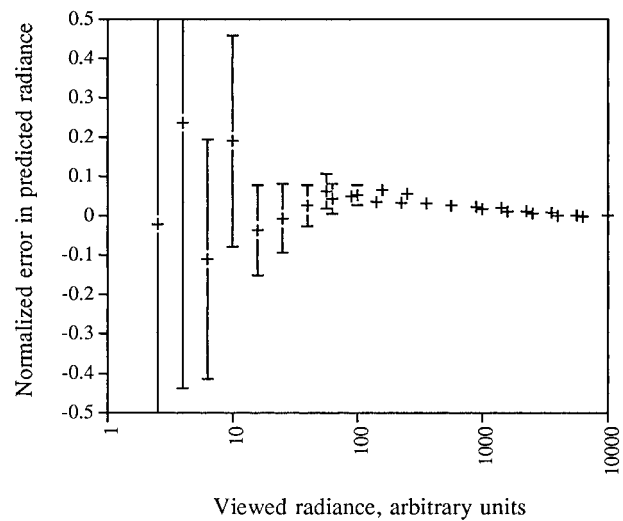


FIG. 2. The normalized deviation from linearity for a linearity test of the imaging aureole radiometry system. The system shows good linearity over more than three orders of magnitude. Standard deviations of the pixel values are displayed as error bars in the y direction.

dark image is acquired. The dark image is then subtracted from the sky data image as the first step in the data processing. In addition to this dark noise, readout noise from the sampling electronics occurs and is difficult to independently estimate or separate from the dark noise. All of the noise factors together result in a standard deviation per pixel of 11 counts.

c. Linearity characterization

Charge-coupled device arrays are inherently linear devices when properly biased. Nevertheless, an experiment was performed to determine the overall system response linearity. The camera imaged a diffusing plaque from a constant distance. The source illuminating the diffuser was then placed at logarithmically spaced distances for each set of exposures in order to achieve the desired plaque irradiances. Such spacing is convenient as the radiance from the plaque varies as the square of its distance from the source and several orders of magnitude can be generated. An image dataset was acquired at each step and an average value from the center 100 pixels was recorded. Figure 2 shows the normalized deviation of the measured radiance from the predicted radiance, that is,

$$\begin{aligned} \text{Normalized error} \\ = \frac{\text{measured radiance} - \text{predicted radiance}}{\text{measured radiance}}. \end{aligned}$$

This was measured over nearly the entire range of the camera, from the dark level to approximately 55 000 counts. The signal was linear to within 5% over three orders of magnitude. The normalized error only increas-

es significantly when the signal minus dark is less than 10 counts, that is, on the order of the system noise.

d. Absolute radiometric flux calibration

In order to determine the absolute spectral response of each CCD pixel, it was necessary to first determine the absolute transmission curve $T(\lambda)$ for each interference–neutral density filter pair. A monochromator (Optronics 740A), configured for 1-nm resolution and checked for offset using known emission lines from a mercury lamp, was used to measure filter transmission. The measurement extended to where the transmission was 10^{-4} of the peak transmittance on each side of the filter's peak transmittance. In addition measurements were made to verify that the out-of-band response was negligible. This was repeated for all four interference filters. The interference filter bandwidths and center frequencies are summarized in Table 1.

Following this, the system was set to view a nearly Lambertian-calibrated Spectralon plaque at 45° off normal. The plaque was illuminated by a 1000-W standard lamp (FEL, spectral irradiance calibration traceable to NIST standards). This provided a known source of radiance for system calibration. The plaque was viewed at 45° to avoid any specular reflections from the surface of the Spectralon. The variation of the reflectance with viewing angle had been previously measured for the particular plaque used (Moore et al. 1998), and these measurements agreed with other measurements in the literature (McGuckin et al. 1997). Thus the manufacturers absolute calibration at a 2° off-normal viewing angle could be related to our 45° viewing angle. An estimate of the uncertainty in this reflectance is 1%.

Unfortunately, the calibrated laboratory radiance source was much dimmer than the solar aureole; the neutral density (ND) filters could not be included in this measurement. The transmission of the neutral density filters was determined in the same manner as the interference filters, and these transmission values were folded into the calibration. Two higher transmittance neutral density filters were measured separately and then combined for each channel so that a better calibration accuracy could be achieved given the signal-to-noise limitations of the test setup. As neutral density filter transmission has nonzero wavelength dependence, the transmission of each filter was determined at wavelengths appropriate for each instrument channel. The accuracy of this measurement is estimated to be 2%. While separating the ND filter from the absolute calibration introduces a possible error source, it was believed that this would introduce less error than substantially increasing the integration time.

An absolute calibration factor was then determined for each pixel, and a matrix was constructed such that when applied pixel by pixel to image data, after dark signal removal, it corrects both for optical rolloff as well as generating a matrix of absolute radiance values.

This procedure is repeated both before and after each field deployment.

e. Absolute radiometric accuracy and precision

Tests were performed to quantify radiometric jitter, that is, repeatability or the lack thereof between measurements. A plaque was illuminated with a steady source and 20 images were acquired. After applying the above calibration procedure to each image, a 100-pixel sample near the center of each image was selected for analysis. The results show that the jitter, that is, radiometric precision, for the entire electromechanical system is on the order of 0.1%. The absolute accuracy of the system is a combination of several factors: the standard lamp (3%), linearity (5%), reflectance plaque (1%), and neutral density filter (2%). These errors combine to a radiometric accuracy of 6%.

f. Optical beam spread function

Inherent in this instrument design is the transformation of angular skylight intensity in the object space to position dependent data in the focal plane array. This is accomplished simply by adjusting the camera lens focus to infinity. For a perfect convergent lens with focus set to infinity, all photons incident at one angle would be mapped to exactly one point in the focal plane. In order to quantify the beam spread function of the aureole radiometry system, a helium–neon laser beam was expanded to a diameter larger than the camera aperture in order to completely fill the instrument aperture and to decrease the divergence of the laser beam. This beam then directly illuminated the camera aperture from a series of angles (0° , 1° , 2° , 3° , 4° , 5° , 6° , and 7°). At each angle an image was acquired. These measurements showed that over 90% of the counts from this parallel beam source were contained within 0.1° from the center of the spot.

4. Data acquisition and reduction

During the data acquisition sequence, upon alignment with the sun, the instrument digitizes and stores a sky radiance image, a dark image, and housekeeping data. This is controlled by a custom real-time interrupt driven computer program coded in the C language and in native assembly language.

To reduce the data, a series of automated data reduction programs were coded. These routines act on a collection of raw data (image and dark) files to remove the dark signal. The resulting images are processed to produce image arrays where pixel values are calibrated radiance, and pixel positions correspond to small solid angle elements of the sky at each point in the instrument's field of view. Following this procedure, the user then decides by visual inspection which images merit further analysis. This step is necessary to filter for cloud

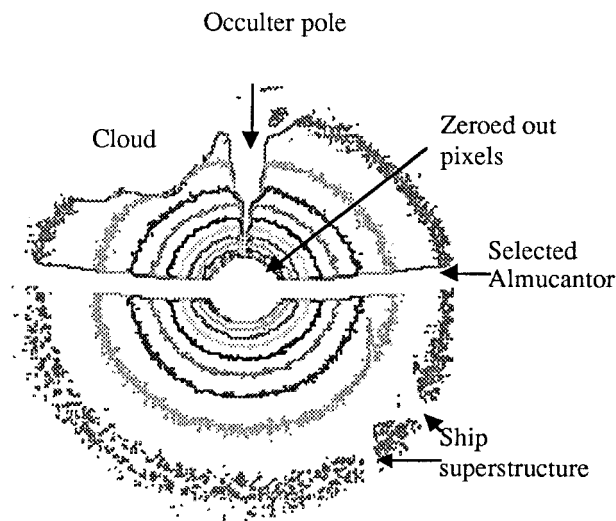


FIG. 3. Sample aureole image radiance contour plot. Some important features in the image are identified.

contamination or measurement artifacts (field-of-view obstruction, flaring, etc.). The next step in the analysis is completed by a series of automated image analysis programs also developed in-house.

The programs open a data file containing a calibrated image. Embedded in this file are coordinates of the pixel closest to the center of the sun, while a separate data file contains solar air mass, instrument channel wavelength mapping, solar constants, Rayleigh, aerosol, and ozone optical depths appropriate for the dataset. A similarly dimensioned (512×512) matrix is generated where each pixel value corresponds to the air mass at the corresponding camera image pixel. An additional matrix is constructed where each pixel value is the scattering angle at the corresponding data image pixel. An example radiance image is shown in Fig. 3.

Due to diffraction effects it is necessary to filter or “digitally occult” some pixels near the image center. The software determines the points, which lie within a small user-definable angle of the sun center, and generates a mask to zero data in the original radiance image array. These occulted pixels are shown as the white circle in Fig. 3. This mask is also applied to the scattering angle and airmass matrices.

It is necessary to ensure sky homogeneity by examining left/right symmetry of radiance versus scattering angle. A typical scatterplot for a “good dataset” displaying this symmetry is shown in Fig. 4. A quantitative symmetry condition is not always used; however, unusable datasets usually have obvious anisotropies. Since small, cloud-free areas around the sun should be used, the most common problems are imaging ship superstructure or thin cirrus clouds. After determining symmetry, it is necessary to resample the almucantar data into appropriately sized solid angle bins. This is accomplished by setting a user-definable (half-cone an-

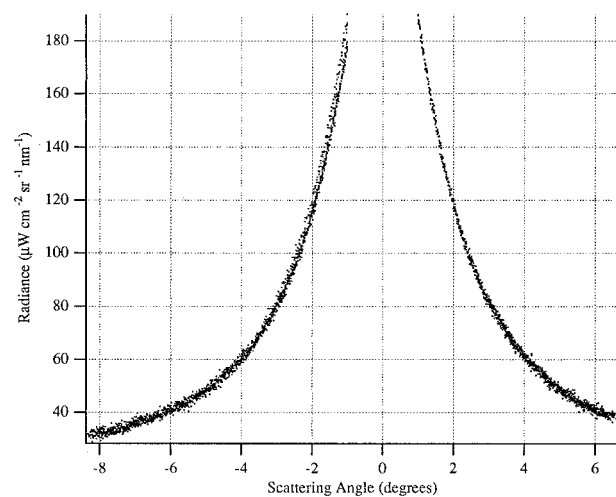


FIG. 4. Plot of the aureole radiance at 670 nm, separating left and right sides of the aureole almucantar. The symmetry of the dataset indicates sky homogeneity, which is necessary for data quality control.

gle) bin size (usually 0.25°) and averaging over all data within that scattering cone, within the appropriate air-mass limits and where the data has not been digitally occulted. Since the sun subtends approximately 0.5° (as viewed from earth), it is unknown whether any individual scattered photon may have come from the left or the right side of the sun. Consequently, there is an inherent uncertainty of 0.5° in scattering angle associated with these aureole measurements. Finer resolution does not significantly increase the information content. It is therefore appropriate to bin radiance data in 0.5° -wide scattering angle bins. The almucantar conic projection on the focal plane array sampled as described is shown as the white band in Fig. 3. An example plot showing the resampled almucantar radiance for the solar aureole is shown in Fig. 5.

As an example of a derived product, Fig. 6 shows an aureole radiance measurement (Ritter et al. 1997b) combined with an almucantar measurement from the Sky Radiance Distribution (SkyRADS) system (Zibordi and Voss 1989). The imaging aureole radiometer supplied the small angle aureole scattering data while the SkyRADS system, which has a wide field of view, supplied the large-angle scattering data. The angle in an aureole image between the sun center and the data point is the scattering angle. This should not be confused with the almucantar azimuth angle (ϕ), which is related to the scattering angle but is also a function of the solar zenith angle. The range in scattering angle (Φ) data is constant and set by the field of view of the instrument. In the case shown the solar elevation was 40° , thus the aureole camera data extends from 1° to above 10° in ϕ . The angle where the sky radiance camera data turns down (approximately 20° in this case) is where the solar occulter in the system begins to block the sky. In this case there is an area between 10° and 20° in Φ where

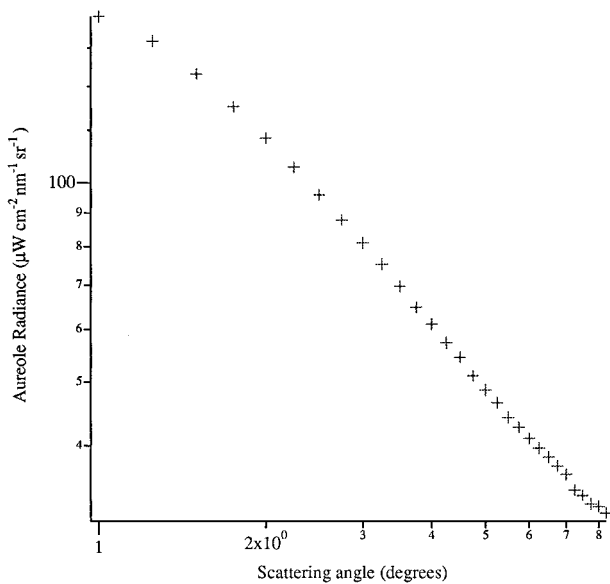


FIG. 5. Resampled aureole almucantar radiance data at 670 nm.

the data must be interpolated between the two systems, as shown in the graph.

5. Conclusions

A new instrument for obtaining absolute radiometric measurements of the solar aureole radiance distribution has been described. Unique to the instrument are the combination of an imaging radiometric instrument, the presence of an image of the solar disk in each image, and the use of a new optoelectronic alignment and triggering system (Ritter 1998). The instrument permits acquisition of the circumsolar sky radiance within 7.5° of the center of the solar disk, and within 1° of the edge of the solar disk. This innovation makes possible, for the first time, reliable and accurate radiometric measurements of the solar aureole from unstable mobile platforms such as ships. These measurements are important as input to atmospheric correction models employed in remote sensing for vicarious satellite sensor calibration, the remote determination of aerosol size characteristics, modeling radiative forcing, and validating aerosol models. This instrument will be used in field studies of atmospheric aerosols and in satellite validation campaigns.

Acknowledgments. The authors are grateful for support from the United States through funding from the NASA Goddard Space Flight Center under Contract NAS5-31363. The authors would also like to thank Howard Gordon, Al Chapin, Bernie Romero, and Edmond Ritter, who provided valuable support.

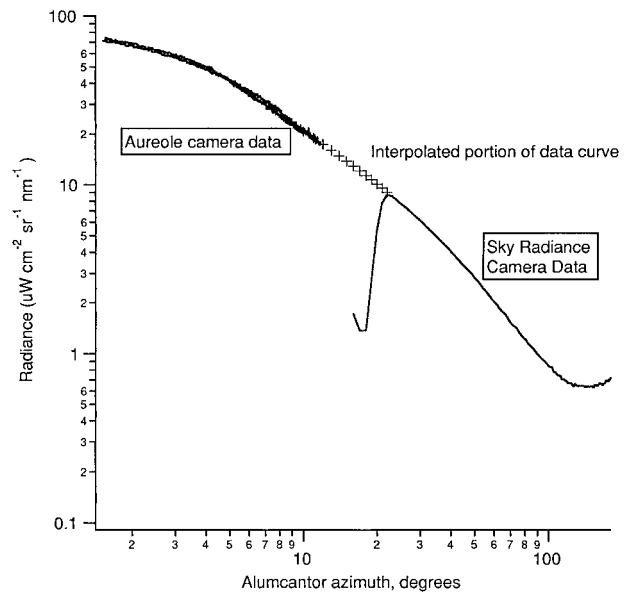


FIG. 6. Example almucantar curve at 860 nm. This includes data from the aureole camera system and the sky radiance camera system. The portion of the almucantar requiring interpolation is shown as crosses in the graph.

REFERENCES

- Charlson, R. J., S. E. Schwartz, J. M. Hales, R. D. Cess, J. A. Coakley Jr., J. E. Hansen, and D. J. Hofmann, 1992: Climate forcing by anthropogenic aerosols. *Science*, **255**, 423–430.
- Clark, D. K., H. R. Gordon, K. J. Voss, Y. Ge, W. Broenkow, and C. Trees, 1997: Validation of atmospheric correction over the oceans. *J. Geophys. Res.*, **102**, 17 209–17 217.
- Gordon, H. R., 1997: Atmospheric correction of ocean color imagery in the Earth Observing System era. *J. Geophys. Res.*, **102**, 17 081–17 106.
- Holben, B., A. Setzer, T. F. Eck, A. Pereira, and I. Slutsker, 1996: Effect of dry-season biomass burning on Amazon Basin aerosol concentrations and optical properties. *J. Geophys. Res.*, **101**, 1992–1994.
- Houghton, J. T., L. G. Meira Filho, B. A. Callendar, N. Harris, A. Kattenberg, and K. Maskell, Eds., 1996: *Climate Change 1995: The Science of Climate Change*. Cambridge University Press, 572 pp.
- McGuckin, B. T., D. A. Haner, and R. T. Menzies, 1997: Multiangle imaging spectroradiometer: Optical characterization of the calibration panels. *Appl. Opt.*, **36**, 7016–7022.
- Moore, K. D., K. J. Voss, and H. R. Gordon, 1998: Spectral reflectance of whitecaps: Instrumentation, calibration, and performance in coastal waters. *J. Atmos. Oceanic Technol.*, **15**, 496–509.
- Nakajima, T., M. Tanaka, and T. Yamauchi, 1983: Retrieval of the optical properties of aerosols from aureole and extinction data. *Appl. Opt.*, **22**, 2951–2959.
- , G. Tonna, R. Rao, P. Boi, Y. J. Kaufman, and B. Holben, 1996: Use of sky brightness measurements from ground for remote sensing of particulate polydispersions. *Appl. Opt.*, **35**, 2672–2686.
- Ritter, J. M., 1998: Remote measurement of aerosol scattering properties and the development of a novel imaging solar aureole radiometer. Ph.D. thesis, University of Miami.
- , K. J. Voss, and H. R. Gordon, 1997a: A new instrument for shipborne radiometric measurements of the solar aureole. *1997 Spring Meeting*, Baltimore, MD, Amer. Geophys. Union, Mineralogical Society of America, and Geochemical Society.
- , —, —, D. Clark, and L. Koval, 1997b: Solar aureole mea-

- measurements of volcanic aerosol in the Kilauea plume. *1997 Fall Meeting*, San Francisco, CA, Amer. Geophys. Union.
- Twomey, S., 1977: The influence of pollution on the shortwave albedo of clouds. *J. Atmos. Sci.*, **34**, 1149–1152.
- Wang, M., and H. R. Gordon, 1993: Retrieval of the columnar aerosol phase function and single-scattering albedo from sky radiance over the ocean: Simulations. *Appl. Opt.*, **32**, 4598–4609.
- Zibordi, G., and K. J. Voss, 1989: Geometric and spectral distribution of sky radiance: Comparison between simulations and field measurements. *Remote Sens. Environ.*, **27**, 343–358.